MATERIALS CHEMISTRY
FRONTIERS

RESEARCH ARTICLE

View Article Online
View Journal | View Issue

Cite this: *Mater. Chem. Front.*, 2024, **8**, 3973

Colloidal fluorine-doped ZnO quantum dots: the synergistic action of atomic doping and growth conditions directs fluorescence and photoactivity†

Noemi Gallucci,[ab] Alessandro Cangiano,[ab] Simone Russo,[c] Giulio Pota,[c] Rocco Di Girolamo,[a] Eugénie Martinez,[d] Nicolas Vaxelaire,[d] Luigi Paduano[ab] and Giuseppe Vitiello *[bc]

Quantum dots are nano-sized semiconductor particles showing peculiar optical properties due to the quantum confinement effect. They can efficiently absorb photons and generate excitons, leading to a stable fluorescence emission decisive to designing light-sensitive devices, or they can exert a pronounced photoactivity that favors their use in photocatalysis and photodynamic fields. Among the inorganic quantum dots, ZnO ones show unique optical and electronic properties together with low toxicity, good biocompatibility, and excellent photochemical stability. These features can be deeply influenced by tuning their size, surface, and/or bulk defects as well as by doping. Doping with anionic atoms represents an intriguing alternative to cationic metals to improve ZnO activity. Here, the emission behaviour and photoactivity of fluorine-doped ZnO quantum dots were simultaneously studied as a function of fluorine content and synthesis conditions (*e.g.*, wet-precipitation or solvothermal) adopted for the fabrication. The obtained results demonstrated that a low fluorine content (<5 nominal at%) was pivotal to induce a significant enhancement of the relative emission quantum yield of quantum dots from the wet-precipitation route, while a high photocatalytic activity was guaranteed for those obtained by a solvothermal strategy due to the bulk distribution of atomic defects.

Received 9th August 2024,
Accepted 30th September 2024

DOI: 10.1039/d4qm00655k

rsc.li/frontiers-materials

Introduction

Quantum dots (QDs) are nano-sized semiconductor particles that exhibit unique properties due to their quantum confinement effects in all dimensions.[1,2] These structures, typically ranging from 2 to 15 nm in diameter, can emit or absorb light at specific wavelengths depending on their size, shape, and composition. Due to their unique electronic structure, QDs can efficiently absorb photons and generate excitons, leading to compositions with bright and stable fluorescence emissions.[2,3] Moreover, their size-dependent bandgap enables light absorption across a broad range of wavelengths, making them valuable components for diverse applications such as light-emitting diodes,[4] solar cells,[5] and photodetectors.[6] Also, the photoactivity of QDs extends beyond conventional optics, with potential applications in photocatalysis and photodynamic therapy, where their ability to generate reactive oxygen species under light irradiation holds promise for environmental remediation and cancer treatment.[7–9]

The properties of QDs are profoundly influenced by synthesis conditions, which encompass parameters such as reaction temperature, precursor concentration, reaction time, solvent choice, surface ligands, and doping agents.[10,11] These factors directly impact the size, shape, composition, crystallinity, and surface chemistry of the QDs, consequently determining their optical, electronic, and structural properties.[12–15] For example, doping agents can play a crucial role in amplifying the optical and photoactivity properties of QDs by introducing controlled impurities and defects into their crystal lattice.[16,17] By incorporating doping agents with appropriate energy levels, such as transition metal ions or rare earth elements into QDs, it is possible to effectively tune the energy bandgap and to extend the range of absorbed and emitted wavelengths, thus broadening the final optical response.[12,17] Additionally, doping can modify the charge carrier dynamics within the QD structure, enhancing the photoactivity and photoresponsivity, which are

[a] *Department of Chemical Sciences, University of Naples Federico II, Via Cintia 4, 80126 Naples, Italy. E-mail: giuseppe.vitiello@unina.it*
[b] *CSGI-Center for Colloid and Surface Science, Via della Lastruccia 3, 50019 Sesto Fiorentino, Italy*
[c] *Department of Chemical, Materials and Production Engineering, University of Naples Federico II, P.le Tecchio 80, 80125 Naples, Italy*
[d] *University of Grenoble Alpes, CEA-LETI, 17 Av. des Martyrs, 38054 Grenoble, France*

† Electronic supplementary information (ESI) available. See DOI: https://doi.org/10.1039/d4qm00655k

crucial for applications such as photocatalysis and photovoltaics.[12,18] Moreover, doping can enhance the stability and quantum efficiency of QDs, making them more suitable for long-term and high-performance applications in fields like display technologies, sensing, and biomedical imaging.[19–23]

Among the inorganic materials used to realize photoresponsive QDs, zinc oxide (ZnO) shows fascinating and unique optical and electronic properties.[24,25] Compared with the traditionally II–VI group quantum dots, such as CdSe and CdTe, ZnO-QDs are cheap and biocompatible with biological systems and have attracted great attention in biological labeling and photocatalytic applications thanks to low toxicity and excellent photochemical stability.[26] In this way, atomic doping emerges as a valuable strategy for fine-tuning many features of ZnO-QDs, and in particular the fluorescence and photoactivity properties (especially their visible emission).[27,28] By substituting Zn and O atoms and/or replacing the atomic vacancies within the bulk structure or on the surface of nanocrystals with specific dopants, such as aluminum, indium, or nitrogen,[29] it is possible to finely control the crystalline structure and the photoinduced performances of QDs to suit specific nanotechnological applications.[30,31] The doping with fluorine (F) was proposed as an interesting strategy to improve the activity of ZnO.[32] Indeed, bringing one electron more than an oxygen atom, fluorine atoms may represent a shallow donor state by exploiting their tendency to fill oxygen vacancies (Vo), which are the prevalent defects in the ZnO crystalline structure. As proposed by theoretical calculations, F atoms could increase the distance between neighbouring Zn, leading to the formation of deep localized electron states, and can act as donors when they fill Vo or as acceptors if they remain interstitials.[33,34]

In this context, the role of synthesis conditions appears decisive in finely tuning the growth and properties of undoped and doped ZnO. In particular, wet-chemical syntheses belonging to the bottom-up approach were widely used to produce ZnO nanomaterials offering a high degree of controllability and reproducibility.[35] Among them, wet-precipitation, solvothermal, templated, self-assembly, and interface-mediated syntheses are the main ones used to produce semiconductor nanomaterials. All of them deal with chemical reactions in the solution phase using precursors under suitable conditions. However, each wet-chemical synthesis method differs from the others, meaning that one cannot find a general rule for these kinds of synthesis approaches. To the best of our knowledge, although several F-doped ZnO-based functional materials have been prepared in various shapes and morphologies, such as nano/meso/microcrystals or thin films, the effect of a synergistic action of synthesis conditions and fluorine doping on the properties of ZnO-QDs was not well-proposed yet.

Our study focused on exploring the optical behaviour and photoactivity of colloidal F/ZnO-QDs. We achieved this by adjusting the doping agent content (between 0 and 20 nominal atomic %) and by implementing two different wet-chemical synthetic routes – wet-precipitation and solvothermal methods, which allowed us to control the surface, morphological, dimensional and structural properties of the nanocrystals. A combined approach of physicochemical techniques allowed us to assess how the photoluminescence and photoactive performances of the resulting F/ZnO-QDs were tuned with the aim of favoring a specific application in sensing and/or photocatalysis.

Experimental section/methods

Materials

Zinc acetate dihydrate (ZAD) $Zn(CH_3COO_2)\cdot 2H2O$ ($\geq$99% purity), ammonium hydrogen difluoride NH_4HF_2 ($\geq$99.999% purity), sodium hydroxide KOH ($\geq$85% purity), triethylamine (TEA) $C_6H_{15}N$ (>99% purity), quinine sulfate monohydrate $C_{20}H_{24}N_2O_2\cdot H_2SO_4\cdot H_2O$ (90% purity), methanol ($\geq$99.8% purity), and ethanol (96% vol.) were purchased from Merck (Germany) and used without further purification.

Synthesis of fluorine/doped ZnO nanoparticles

Wet-precipitation method. Undoped (ZnO-QDs) and fluorine/doped ZnO (F/ZnO-QDs) quantum dots were first prepared by adapting a synthesis protocol defined by Beek *et al.*[36] Specifically, the precursor salt, ZAD, was solubilized in methanol to obtain a 0.11 M solution. This was heated at 60 °C, which is a temperature close to the boiling temperature of methanol, equal to 64.7 °C. An appropriate amount of doping salt NH_4HF_2 (corresponding to a nominal content ranging between 0 and 20 at%) was opportunely added to the mixture to induce the formation of nanocrystals including fluorine atoms.[33,34] Different compositions were considered as detailed in Table S1 (ESI†). After the temperature stabilization, a 0.4 M KOH solution was added drop by drop as a basifying and morphologic agent to induce the formation of size-controlled nanocrystals. The resulting solution was stirred for 2 h at 60 °C. The reaction mixture was slowly cooled down to room temperature, then placed in 50 mL centrifuge tubes and centrifuged at 5000 rpm for 5 minutes to separate the supernatant from ZnO-QDs. They were re-dispersed in methanol, and the centrifugation step was repeated twice to wash out all the unreacted substances. Finally, undoped and doped ZnO-QDs were collected in methanol.

Solvothermal method. Undoped ZnO-NCs and F/ZnO-NCs nanocrystals were also synthesized by adapting a protocol previously proposed.[33,34] In detail, 0.528 g of ZAD was dissolved in 144 mL of ethanol, and then 3.36 mL of TEA was introduced into the system at room temperature as a capping agent. After the complete dissolution of the inorganic precursor, 16 mL of bi-distilled water was added to induce hydrolysis and condensation reactions. An appropriate amount of doping salt NH_4HF_2 (corresponding to a nominal content ranging between 0 and 20 at%) was opportunely added to the reaction mixture, as detailed in Table S2 (ESI†). After the doping agent addition, each suspension was transferred into a Teflon recipient, and placed in a circulating over at 120 °C for 2 h. The final mixture was cooled to room temperature, then placed in 50 mL centrifuge tubes, and centrifuged at 10 000 rpm for 5 minutes, to separate the supernatant from ZnO nanocrystals. The obtained nanocrystals were finally dispersed and stored in ethanol.

Physicochemical analysis

Transmission electron microscopy (TEM). TEM images were acquired using the FEI TECNAI G2 200 kV microscope. For all samples, approximately 10 μL of each sample were placed on a carbon-coated copper grid and allowed to air dry before imaging. Images were taken at various magnifications for each sample, from the lowest magnification to have an overall view of the sample at the highest magnification to allow a statistical analysis of the size of the synthesized nanocrystals. The images were processed with a free digital imaging processing system, ImageJ.[37–39]

Dynamic light scattering (DLS). DLS measurements were performed to measure the size of F/ZnO-QDs and F/ZnO-NCs in suspension with a home-made instrument composed of a Photocor compact goniometer (Moscow, Russia), SMD 6000 Laser Quantum 50 mW light source (Laser Quantum, Fremont, CA, USA) operating at 532.5 Å, a photomultiplier (PMT-120-OP/B) and a correlator (Flex02-01D) from Correlator.com (Shenzhen, China). The experiments were carried out on 1 mL of a nanoparticle suspension at a constant temperature (25.0 ± 0.1) °C, by using a thermostatic bath and at the scattering angle θ of 90°.[37–42]

X-ray diffraction (XRD). XRD measurements were carried out to investigate the crystalline structure of F/ZnO samples, by using the Empyrean instrument from Malvern Panalytical (Cambridge, UK). The X-ray source is Cu, λ = 1.54 Å, 45 kV, and 40 mV. The spectra of F/ZnO powders were collected in the 2θ range between 20 and 80 degrees.

X-ray photoelectron spectroscopy (XPS). The surface properties of F/ZnO samples were investigated *via* XPS analysis, which was carried out using a spectrometer VersaProbe II with a monochromatic Al Kα X-ray source ($h\nu$ = 1486.6 eV), a spot of 200 μm, and a dual-beam system (Ar+ e$\bar{e}$) for charge compensation. The pass energy was set at 23.5 eV, leading to an overall energy resolution of 0.6 eV. Photoelectrons were collected at a take-off angle of 45°, which means a sampling depth of approximately 5 nm. The decomposition of the spectra was done using Voigt functions after Shirley's background subtraction with the Multipak software.[38]

UV-Vis spectroscopy. UV-Vis spectroscopy measurements were performed using a Jasco V-560 UV-Vis instrument, a dual-beam instrument, equipped with a deuterium lamp (190–350 nm) and a halogen lamp (330–900 nm). 1.5 mL of suspension containing the F/ZnO was placed in a quartz cuvette to carry out the measurements (optical path: 1 cm, bandwidth: 2.0 nm, and scanning speed: 40 nm min^{-1}).[39]

UV-Vis diffuse reflectance spectroscopy (DRS). UV-Vis DRS measurements were carried out using a UV-2600i UV-VIS spectrophotometer, 230 V (Shimadzu, Milan, Italy), equipped with an integrating sphere ISR-2600Plus operating in a wavelength range of 220–1400 nm. Barium sulfate was used as a reflectance standard. The measured intensity was expressed as the value of the Kubelka–Munk function, $F(R)$, while the direct band-gap energy value was evaluated according to the Tauc-plot linearization of $(F(R)h\nu)$ against $h\nu$.[37,38]

Fluorescence spectroscopy. Fluorescence spectra were recorded at 25 °C using a Horiba Scientific Fluoromax-4 spectrofluorometer equipped with a Peltier control system and 1 cm path length cells. Each F/ZnO suspension was excited to the specific absorption wavelength, determined using UV-Vis spectroscopy measurements (integration time: 0.1 s, excitation and emission slit width: 5 nm). For a correct determination of the relative emission quantum yield, each measurement was performed on three independent samples of both F/ZnO system and quinine monohydrate used as the standard reference. All systems were excited at the maximum absorption (maximum value of 0.3) wavelength determined by UV-Vis spectroscopy measurements, while the standard was excited at 317 nm. These analyses were performed using the following experimental set-up; integration time: 0.1 s, excitation, and emission slit width: 2 nm.[39,40]

Photoactivity under UV-light irradiation. The redox activity of undoped and F/ZnO nanocrystals was assessed by monitoring the degradation of Rhodamine B (RhB) in the dark and under UV-Vis light irradiation. In detail, 100 μg of ZnO-NCs were dispersed in 1 mL of an 8 μg mL^{-1} RhB solution. The mixture was sonicated for five minutes at room temperature and then magnetically stirred. For the photodegradation testing, a high-pressure mercury vapor lamp (Helios Italquartz) with a nominal output of 125 W was utilized.[37,43] Both the visible and UV ranges are covered by the emission lamp, which occurs at 404.7 and 435.8 nm in the visible spectrum. A thermostatic bath (Falc GTR 90) was utilized to maintain a constant temperature of 25 °C while the lamp operated over its full emission spectrum. The lamp was housed inside a quartz sleeve. Each suspension underwent a 5-minute, 1000-*g* centrifugation after testing. The absorbance of the supernatants was measured with a Shimadzu (Milan, Italy) UV-2600i spectrophotometer at 230 V. The rate of degradation $D(t)$% at time t was calculated according to eqn (1):

$$D(t)\% = \frac{A_t - A_0}{A_0} \times 100 \quad (1)$$

where A_t and A_0 are the absorbances of the supernatants at time t and 0, respectively. OriginPro software was used to fit the experimental data obtained by the photocatalytic tests. The estimation of the kinetic parameters was realized by considering valid all the fittings with $R^2 > 0.999$ e $\chi^2 < 10^{-13}$.

Results and discussion

Morphological and dimensional features of F/ZnO

The formation of F/ZnO through both the adopted synthetic routes was proven by morphological and dimensional analyses. As reported in Fig. 1 and Fig. S1 (ESI†), TEM images clearly showed dramatic changes in the morphology and size of undoped and doped ZnO depending on the synthesis conditions and as a function of the amount of doping salt used during the syntheses. In the case of the ZnO-QDs synthesized through the wet-precipitation method, undoped ZnO-QDs (F0/ZnO-QDs) showed a pseudo-spherical morphology with a mean size of ~3 nm in radius (Fig. 1A). These morphological and dimensional properties were obtained for F/ZnO-QDs with a nominal F content in the range 1–7.5 at% (Table S3, ESI†),

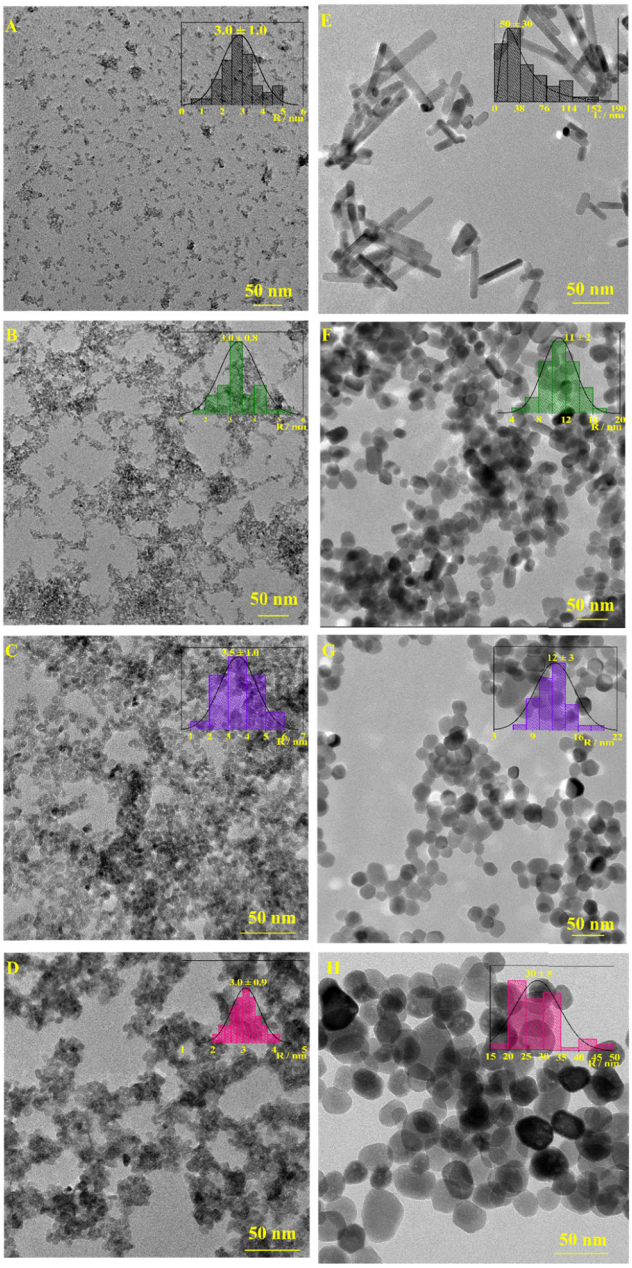

Fig. 1 TEM images of undoped and F-doped ZnO were obtained through the two synthetic approaches: F0/ZnO-QDs (A), F5/ZnO-QDs (B), F7.5/ZnO-QDs (C), F15/ZnO-QDs (D), F0/ZnO-NCs (E), F5/ZnO-NCs (F), F7.5/ZnO-NCs (G), F15/ZnO-NCs (H).

although they showed an increasing tendency to form disordered nanoclusters (Fig. 1A–C and Fig. S1A–E, ESI†). By increasing the fluorine content, QDs with an irregular morphology and a slightly increased size were obtained (Fig. 1D and Fig. S1F–H, ESI†). Moreover, it gradually became almost impossible to distinguish the borders of the single QDs, which resulted in assembled and strongly interconnected as demonstrated by the formation of very irregular clusters with a final morphology like small bushes. This effect was directly related to F content and indicated that the relative composition of the synthesis mixtures drove differently the growth of ZnO-QDs, favoring self-aggregation.

On the other hand, ZnO-NCs synthesized through the solvothermal method showed many differences in morphology and size as a function of doping. Specifically, undoped ZnO nanocrystals (F0/ZnO-NCs) were characterized by a rod-like shape with a rod length $\langle L \rangle$ equal to about 50 nm (Fig. 1E). This evidence indicated that the solvothermal synthesis, although realized for the same time as the wet-precipitation route, hindered the formation of confined quantum dots thus favoring the growth of nanocrystals into nanorods with higher dimensions (Table S3, ESI†), similar to what was previously achieved for a comparable synthesis strategy.[44] The presence of the doping salt drove the formation of pseudo-spherical nanocrystals with a mean radius of ∼30 nm for the F1/ZnO-NCs sample (Fig. S1J, ESI†) and of ∼10 nm with the increase of the fluorine content (Fig. 1F, G and Fig. S1K–M, ESI†). By increasing the atomic percentage of the doping agent, the morphology of nanoparticles varies further, allowing the statistical determination of a length of about 30 nm for F10/ZnO-NCs (Fig. S1N, ESI†) and F15/ZnO-NCs (Fig. 1H) samples. Finally, F20/ZnO-NCs systems showed a heterogeneous character with the prevalence of spheroidal nanoparticles of ∼50 nm in radius (Fig. S1P, ESI†) together with microstructures.

The obtained results confirmed that the incorporation of F^- ions into ZnO seeds influenced the growth of the host lattices. Also, the relative concentration of dopant precursor in the reagents represented a key factor that resulted in initial growth seeds with different crystallographic phases and shapes, leading to doped nanocrystals with different structures and morphologies.[45,46] This evidence agreed with those of mechanistic reports describing the effect of the mostly studied doping with cationic species on the primary stage of semiconductor nanocrystal growth.[47,48]

The colloidal behavior of F/ZnO systems in alcohol suspension was investigated by DLS measurements (Fig. S2, ESI†) with the aim to verify if the clustering process was only due to the solvent evaporation occurring during TEM analysis or if F/ZnO exerted a natural tendency to self-aggregate as a function of their morphology and composition. Hydrodynamic radius distributions revealed the presence of a single population in all the samples, except for the F0/ZnO-NCs system, which showed two populations with R_h of ∼100 and 600 nm, respectively. This behavior can be explained as due to the very different morphology and size of such nanocrystals, which favored their clustering and the subsequent increased colloidal instability. At greater F contents, R_h increased moving from F0/ZnO-QDs to F2.5/ZnO-QDs and remained constant for F5/ZnO-QDs and F7.5/ZnO-QDs. R_h values of F10/ZnO-QDs and F15/ZnO-QDs were smaller than those of samples with less fluorine, being about 28 nm, while for a population with a hydrodynamic radius value of about 62 nm was observed F20/ZnO-QDs sample. In contrast, for samples obtained through the solvothermal method, the self-aggregation process was not controllable with the formation of aggregates with R_h ranging in 75–300 nm, not following any specific trend as a function of fluorine content and confirming that the process of self-aggregation was not a controllable process.

Structural and chemical features of F/ZnO

As shown in Fig. 2A, B and Fig. S3A, B (ESI†), XRD patterns of all F/ZnO nanosystems indicated the presence of typical peaks of wurtzite crystalline structure (JCPDS 36-1451). This was quantitatively confirmed by the values of the diffraction angles (2θ), the cell dimensions (a, b, c, α, β, and γ), and Miller indices (hkl) of the peaks, as listed in Table S4 (ESI†). Any shift of the diffraction peaks resulted from the experimental data of doped *versus* undoped samples, suggesting that any distortion of the crystalline lattice of ZnO occurred because of the presence of the doping agent and the synthesis method. However, the presence of diffraction peaks corresponding to a second different crystalline phase was detected in the diffraction spectra of samples obtained using a high amount of doping salt (from F7.5/ZnO-QDs to F20/ZnO-QDs). It could be ascribable to the presence of ZnF_2 (indicated by stars in Fig. 2A) in the tetragonal crystalline structure with spatial group $P4_2/mnm$ was also observed. The formation of ZnF_2 may be a direct consequence of the dissociation of the fluorine-based doping salt, NH_4FHF, into H^+, HF_2^-, and HF species occurring in the reaction mixture. The HF specie was able to react with $Zn(CH_3COO)_2$ salt, inducing a competitive reaction $Zn(CH_3COO)_2 + 2HF \rightarrow ZnF_2 + CH_3COOH$ which led to the formation of ZnF_2.[49] At the same time, these species could exert a corrosive action toward the nanocrystal surface exposed to the solution, probably contributing to the definition of the irregular morphology of QDs. Although these phenomena were secondary concerning the formation of the ZnO phase, they became very decisive at the highest nominal content of the doping agent (F10/ZnO-QDs to F20/ZnO-QDs) in causing the deepest morphological differences and highest tendency to form disordered clusters, as indicated by TEM and DLS. These results confirmed that both the synthesis conditions and the relative amount of doping agent strictly influenced the chemical process of nanocrystal growth, simultaneously tuning the crystalline structure, shape, and size of F/ZnO.

The XPS analysis led to the description of the surface chemical composition of doped ZnO nanocrystals compared to the undoped ones. The spectra reported in Fig. 2C, D and Fig. S3C, D (ESI†) showed the characteristic peaks of ZnO (Zn 2p, Zn 3s, Zn 3p, Zn 3d, and O 1s) for all the samples, while in those with the highest nominal F concentration (F15/ZnO-QDs

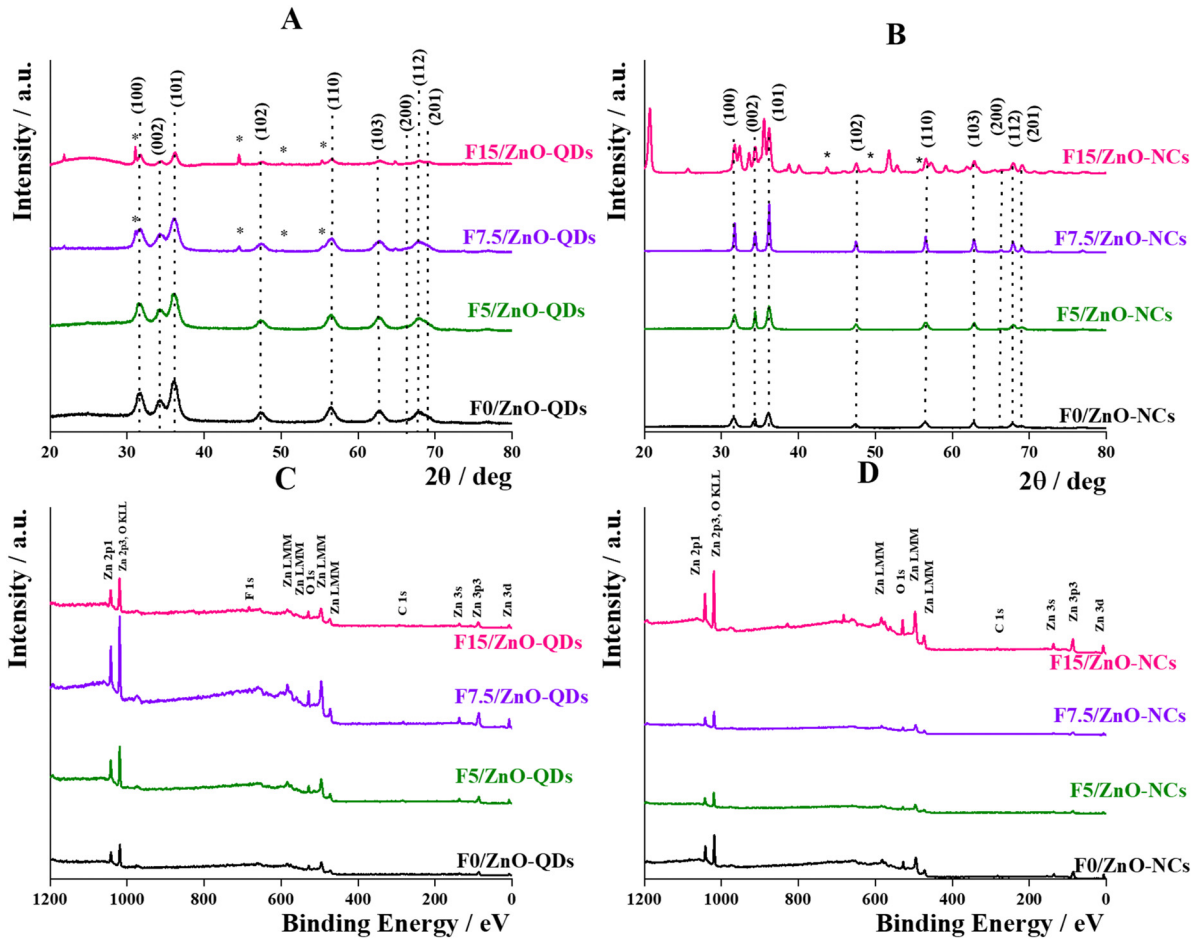

Fig. 2 XRD patterns of undoped and F-doped ZnO-QDs as synthesized through the wet-precipitation method (panel A) and of undoped and F-doped ZnO-NCs as synthesized through the solvothermal method (panel B). Dot lines indicate ZnO peaks, while stars indicate the ZnF_2 ones; and XPS patterns of undoped and F-doped ZnO-QDs as synthesized through the wet-precipitation method (panel C) and undoped and F-doped ZnO-NCs as synthesized through the solvothermal method (panel D).

and F20/ZnO-QDs), the F 1s peak was visible. The very small C 1s peak was ascribable to carbon contamination, probably due to the presence of unconverted reagents and/or of reaction by-products not completely removed during the purification step. A quantitative determination of the chemical species was also realized by a deeper analysis of the main XPS peaks, such as Zn 3p, O 1s, F 1s, and C 1s (Fig. S3, ESI†). The spectrum of Zn 3p (Fig. S3A and B, ESI†) showed two peaks related to the two components of the $Zn3p_{3/2}$–$Zn3p_{1/2}$ doublet located at 87 and 90 eV respectively. The XPS spectrum of O 1s (Fig. S3C and D, ESI†) also presented two peaks: (i) one between 529 and 530 eV, due to the oxygen bound to zinc, and (ii) the other one at about 532 eV, due to the oxygen bound to carbon and fluorine. In all the cases, the intensity of the O–Zn peak was higher than that of the O–C/O–F peak, except for the F15/ZnO-QDs and F20/ZnO-QDs samples. The peak of F was visible and, therefore, its concentration was quantifiable only for the highest nominal concentration samples obtained through the wet synthesis (Fig. S3E and F, ESI†). Finally, as previously indicated, the C 1s signal (Fig. S3G and H, ESI†) was due to the presence of an unconverted reagent as well as to the K 2p signal (Fig. S3G, ESI†) which was detected only in the samples with the highest F amount. By integration of these peaks, the atomic composition of the different F/ZnO was estimated, as summarized in Table 1.

For all F/ZnO nanocrystals, no significant changes were observed in the surface atomic concentration of Zn as well as of C and both C-bonded and Zn-bonded O species. Only in the case of F15 and F20 samples for both syntheses, a lower concentration of O–Zn species with respect to the other samples was detected, suggesting that the content of oxygen vacancies (Vo) on the nanocrystal surface was greater. The presence of F atoms was not detectable below the XPS sensitivity ($\sim$1 at%). Indeed, the presence of F atoms on the surface of F/ZnO-QDs synthesized through the wet method (up to F5/ZnO-QDs) resulted in approximately equal to $\sim$1.5 at% for F5 and F7.5, $\sim$7–8% from F10 to F20 samples. Instead, for F/ZnO-NCs samples synthesized through the solvothermal method (up to F10/ZnO-NCs), the F content was estimated to be $\sim$4 at% for F10, $\sim$9–13 at% for F15 and F20 nanocrystals. These results indicated an increasing amount of surface defects. This probably indicated that a concentration of 7/8 at% (wet-precipitation method) and of 9/13 at% (solvothermal method) is the maximum concentration of dopant that ZnO may exhibit on the surface. However, in the case of ZnO-QDs from wet-precipitation synthesis, it is plausible to consider that the F content estimated from the XPS analysis may represent the effective one, given that the QDs diameter ($\sim$5 nm) was compatible with the penetration depth of the beam used for analyses. Instead, in the case of solvothermal ZnO-NCs, these results could indirectly suggest that the monovalent anionic species were partially included in the crystalline structure by replacing the oxygen vacancies,[33] and not only localizing on the surface.

Optical features of F/ZnO: absorption, emission, and relative quantum yield

UV-Vis and fluorescence spectroscopy measurements were carried out to define the optical properties of F/ZnO as a function of size and fluorine relative content.

All F/ZnO samples showed an absorption behavior in the UV region exerting with a peak ranging between 332 and 361 nm, with changes directly related to the preparation methods, and consequently to nanocrystal size and fluorine content. Indeed, the quantum dots synthesized by the wet-precipitation (Fig. 3A) showed a maximum absorption centered between 332 and 347 nm, while a redshift was observed for nanocrystals obtained through the solvothermal method (Fig. 3D), with a maximum at $\sim$360 nm. This effect is ascribable to the greater size of such nanocrystals in agreement with previous results.[50,51]

Fig. 3B, E and Fig. S5 (ESI†) reported the Tauc plot reflectance data for the different F/ZnO samples. They were deduced using Tauc formulae and Kubelka–Munk function $F^{®}$ and expressed in eqn (2) and (3) respectively,

Table 1 Atomic concentrations of Zn, O, C, and F as obtained by the XPS spectra

Sample	Zn at%	O (O–Zn) at%	F at%	C at%	O (O–C) at%
Wet-precipitation synthesis					
F0/ZnO-QDs	31 ± 6	31 ± 6		14 ± 3	24 ± 5
F1/ZnO-QDs	33 ± 6	27 ± 5		18 ± 3	22 ± 4
F2.5/ZnO-QDs	33 ± 7	25 ± 5		18 ± 4	23 ± 5
F5/ZnO-QDs	36 ± 7	27 ± 5	1.5 ± 0.3	17 ± 3	19 ± 4
F7.5/ZnO-QDs	39 ± 8	27 ± 5	1.7 ± 0.3	15 ± 3	17 ± 3
F10/ZnO-QDs	40 ± 8	29 ± 6	7 ± 1	15 ± 3	16 ± 3
F15/ZnO-QDs	31 ± 6	13 ± 3	8 ± 2	14 ± 3	24 ± 5
F20/ZnO-QDs	35 ± 7	19 ± 4	7 ± 1	17 ± 3	23 ± 5
Solvothermal synthesis					
F0/ZnO-NCs	41 ± 8	28 ± 5		15 ± 3	15 ± 3
F1/ZnO-NCs	37 ± 7	24 ± 5		21 ± 4	18 ± 4
F2.5/ZnO-NCs	42 ± 8	27 ± 5		11 ± 2	20 ± 4
F5/ZnO-NCs	38 ± 8	31 ± 6		15 ± 3	16 ± 3
F7.5/ZnO-NCs	39 ± 8	29 ± 6		17 ± 3	15 ± 3
F10/ZnO-NCs	41 ± 8	26 ± 5	4.2 ± 0.8	9 ± 2	19 ± 4
F15/ZnO-NCs	40 ± 8	18 ± 3	9 ± 2	6 ± 1	26 ± 5
F20/ZnO-NCs	38 ± 8	10 ± 2	13 ± 3	7 ± 1	32 ± 6

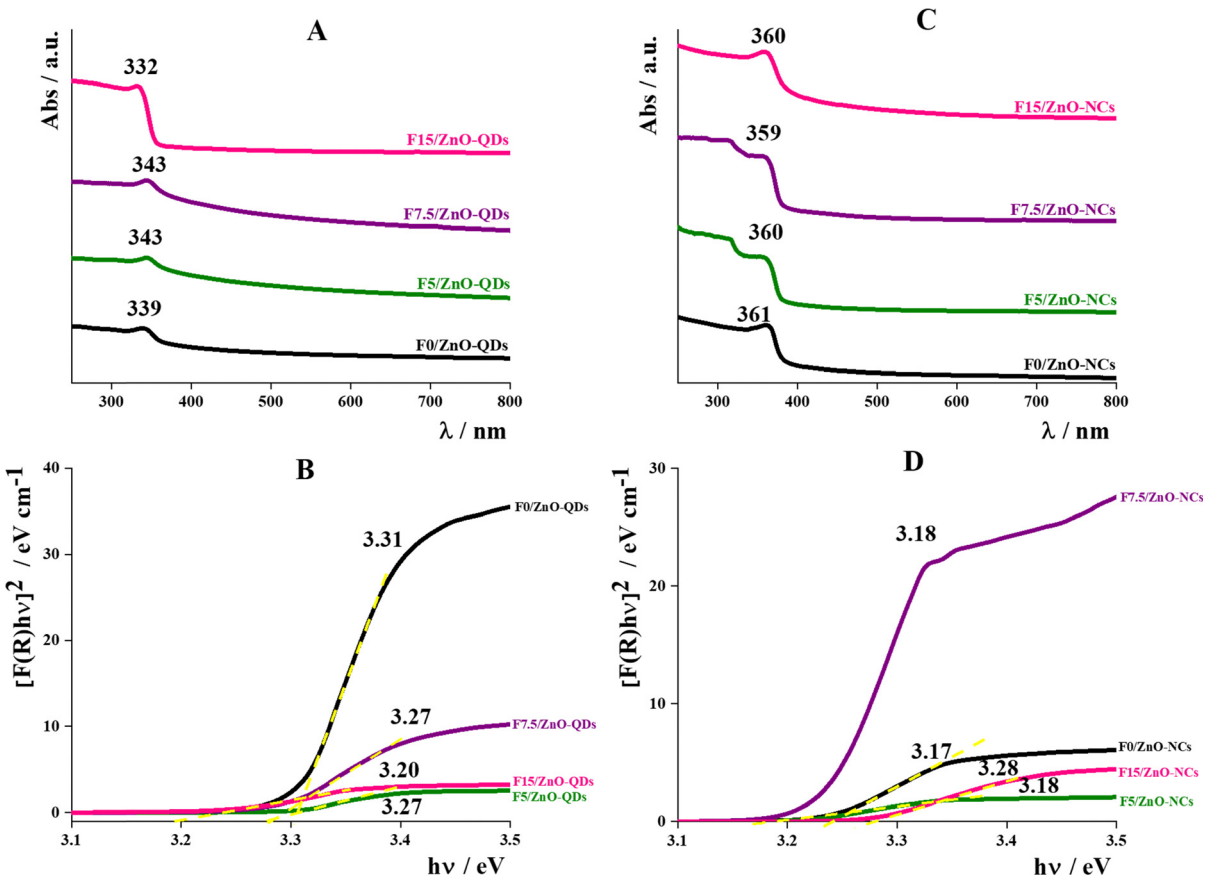

Fig. 3 UV-Visible spectra of undoped and F-doped ZnO as synthesized through the wet-precipitation method (panel A) and the solvothermal method (panel C); Tauc plot of undoped and F-doped ZnOs as synthesized through the wet-precipitation method (panel B) and the solvothermal method (panel D).

$$(\alpha \times h\nu)^n = B(h\nu - E_g) \quad (2)$$

$$F(R) = \frac{K}{S} = \frac{(1-R)^2}{2R} \quad (3)$$

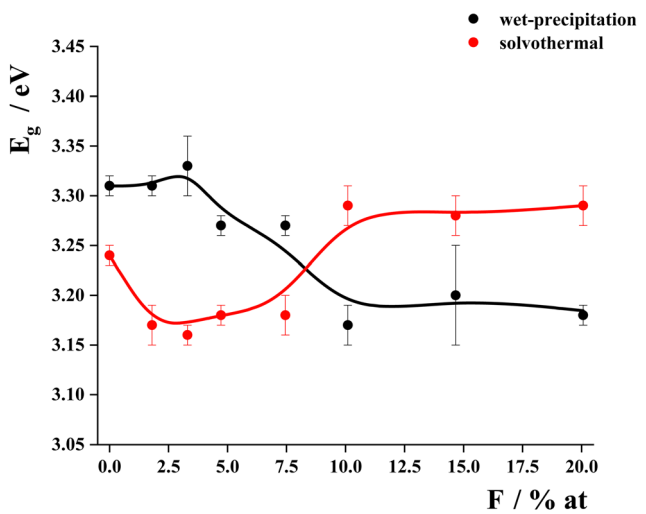

Fig. 4 Band-gap energy values obtained from the Tauc-plot and relative quantum yield for all F/ZnO systems.

where R is the reflectance, $F(R)$ is the Kubelka–Munk function, proportional to the absorption coefficient α, $h\nu$ is the photon energy, E_g is the optical bandgap, B is a constant and n is a constant that determines optical transition type, $n = 2$, for direct transition commonly considered for ZnO, respectively. The bandgap energy (E_g) is an important parameter for the definition of the properties of a semiconductor. The trends of E_g values as a function of the F atomic% are shown in Fig. 4.

By the inspection of Fig. 4, it is possible to note that the relative doping concentration strongly affected the optical properties of F/ZnO. Indeed, the maximum absorption wavelength of F0/ZnO-QDs, F1/ZnO-QDs and F2.5/ZnO-QDs, for which XPS had not detected the fluorine presence, increased as the R_h of suspended aggregates increased, as also observed by Xu *et al.* for undoped ZnO-QDs with a dimension between 15 and 40 nm.[52] F5/ZnO-QDs and F7.5/ZnO-QDs (with an estimated F amount of 1.5 and 1.7 at%, respectively) had a maximum at about 343 nm, as well as the same F concentration shifted the maximum peak in F10, F15 and F20 ZnO-QDs at about 333 nm. It is interesting to note that the increased concentration of the doping agent caused a decrease in the absorption maximum, as already observed by Singh *et al.* doping ZnO nanoparticles with Mn and observing a blueshift from 366 to 352 nm by increasing the Mn concentration from 1

to 4%.[53] The same trend was also observed by Hammad *et al.* for Co-doped ZnO nanoparticles.[54]

Instead, a redshift can be observed for samples synthesized through the solvothermal method. This shift is typical of doped zinc oxide nanoparticles and increases with the amount of doping agent.[19,20,55] The presence of defects and doping agent also affected the bandgap values of F/ZnO. For undoped ZnO, it was 3.31 eV for F0/ZnO-QDs and about 3.24 eV for F0/ZnO-NCs, which was slightly lower than that of ZnO bulk (3.37 eV) and can be explained as due to the presence of defects in the crystalline structure of nanocrystals.[56,57] Then, F1/ZnO-QDs and F2.5/ZnO-QDs samples showed values comparable to that of F0/ZnO-QDs, which confirmed the results of XPS that do not detect the presence of F in these samples. In the case of F5/ZnO-QDs and F7.5/ZnO-QDs samples, E_g was equal to 3.27 eV; this decrease, if compared to the values of previous samples, was due to the presence of the doping agent at low amounts (1.5 and 1.7 at%, respectively) as indicated by XPS analysis. Indeed, the presence of the fluorine doping agent can create a new valence band causing a decrease in the bandgap value.[58] Finally, the bandgap of F10/ZnO-QDs, F15/ZnO-QDs, and F20/ZnO-QDs samples was even lower, probably due to a greater concentration of fluorine anions. These values agreed with the shift of the maximum absorption peaks observed for F/ZnO-QDs in suspension. Instead, the bandgap of doped ZnO-NCs synthesized by the solvothermal method was lower than that of the undoped ones but, in all cases, the value was equal to about 3.17 eV, except for F10/ZnO-NCs, F15/ZnO-NCs, and F20/ZnO-NCs samples prepared with a greater nominal amount of fluorine doping agent. This evidence confirmed that the changes in the electron structures depended not only on the dopant amount but also on the size and shape of nanocrystals as driven by preferential growth way due to the specific synthesis method.[34,59]

Fluorescence spectra were recorded in the 400–700 nm range by exciting each sample at the maximum absorption wavelength as determined by UV-Vis analysis. All emission spectra of F/ZnO-QDs synthesized by wet-precipitation (Fig. 5A, B and Fig. S7, ESI†) showed a single band centered at about 530 nm that can be attributed to the presence of point defects, such as oxygen vacancies or interstitial oxygen, directly related to emission peaks and affecting the fluorescence intensity. An emission band between 500 and 520 nm was ascribable to oxygen vacancies V_O; a band between 550 and 560 nm to interstitial oxygen O_i; a band between 400 and 440 nm to zinc vacancies V_{Zn} and interstitial zinc Zn_i.[60–63] The green emission could be associated with a transition between V_O and holes.[64] The intensity of these broad bands depends on the number of luminescence centers and the recombination of the electron–hole pairs.[20,33] In the range of 1 to 7.5%, the fluorescence

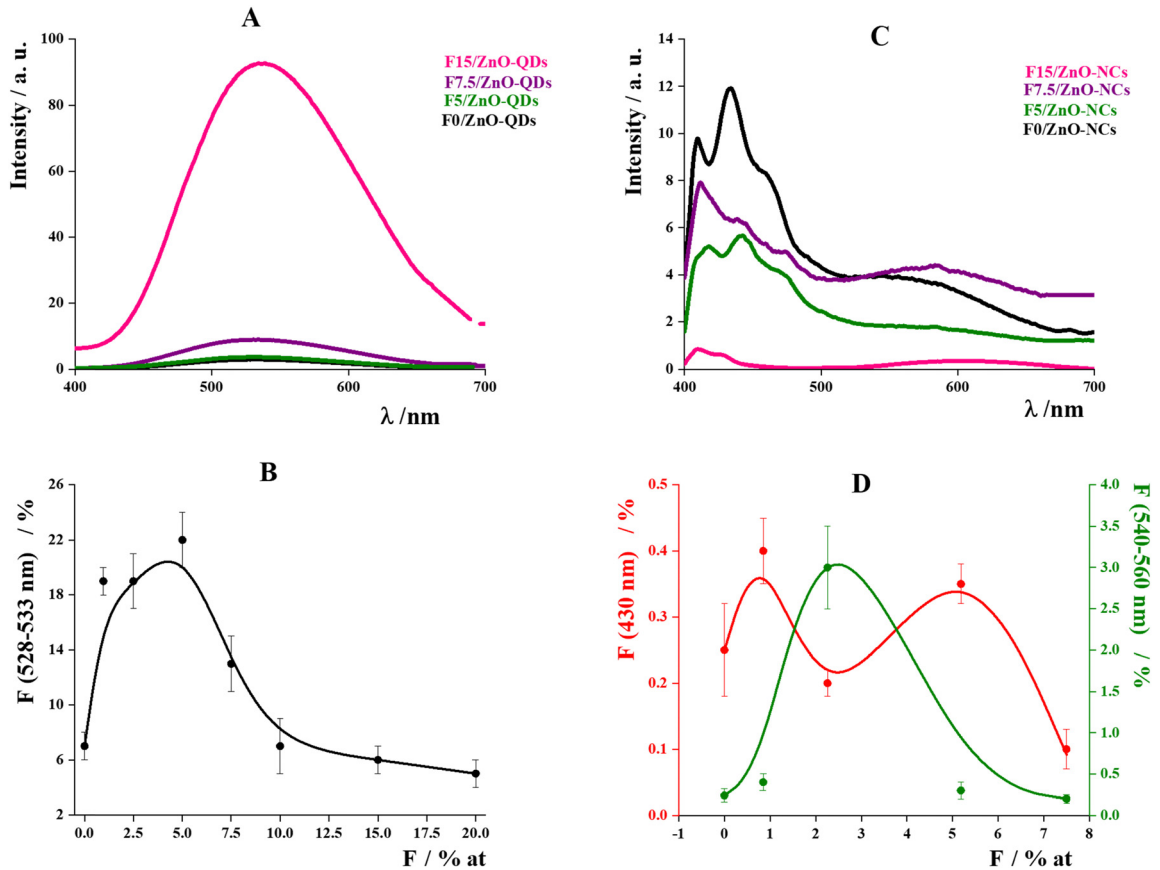

Fig. 5 Fluorescence spectra and relative quantum yield values of undoped and F-doped ZnO as synthesized through the wet-precipitation method (A) and (B), respectively or the solvothermal method (C) and (D), respectively.

intensity decreases with increasing dopant, due to the decrease in the Vo number, since the F atoms fill V_o sites.[33] The trend is not linear for the last three samples of the series, probably due to the presence of another crystalline species, as demonstrated by XRD data. Instead, the emission spectra of F/ZnO nanocrystals synthesized through the solvothermal method (from F0/ZnO-NCs to F7.5/ZnO-NCs) resulted in more complex with the presence of multiple peaks which were identified by a Gaussian peak deconvolution as shown in Fig. S8 (ESI†).

This approach highlighted that the emission of F/ZnO-NCs consists of several contributions. For all analyzed systems (F0/ZnO-NCs–F7.5/ZnO-NCs), four different peaks were identified, together contributing to the fluorescence behavior of these nanocrystals. The comparison of experimental and fitted spectra indicated that the doping agent did not influence the optical properties. Consequently, it is plausible to consider that a key role was played by the structural characteristics of ZnO nanocrystals given by the synthetic protocol.[65] Indeed, ZnO nanocrystals are characterized by various kinds of defects, which are directly related to the features of their fluorescence emission spectra. Especially, defects such as zinc vacancies (V_{Zn}) and interstitial zinc (Zn_i) were widely recognized as responsible for the emission in the region of 400–440 nm.[60] However, the origin of the broad emission band in the 540–560 nm region was still the subject of debate in the scientific community. In particular, two kinds of defects, such as oxygen vacancies (V_O) and interstitial oxygen (O_i), can be considered as possibly responsible for this emission band,[61,63] acting as acceptor and donor punctual defects, respectively. Carefully analyzing the experimental data obtained in this work and the scientific literature can be inferred that the V_O was pointed out as responsible for the "green" emission band (large emission band between 500 and 520 nm) of ZnO-NPs; hence, the emission band observed in the systems here (emission band centered at 550 nm) can be attributed to O_i occupying octahedral sites,[66,67] as more thermodynamically stable than tetrahedral O_i.[61]

To quantitatively estimate the changes in fluorescence emission, the relative quantum yield (Φ) with respect to the quinine sulfate chosen as a standard was determined by following the analytical procedure as described in the ESI.† The trends of the experimental values are reported in Fig. 5C and D. In the case of ZnO-NCs, the relative quantum yield is not affected by the presence of the doping agent, in fact, in all cases, it is less than 3%. Conversely, relative quantum yield increases with the fluorine content up to the sample F5/ZnO-QDs, which by XPS analysis has an atomic percentage of F on the QDs surface of 1.5% at,

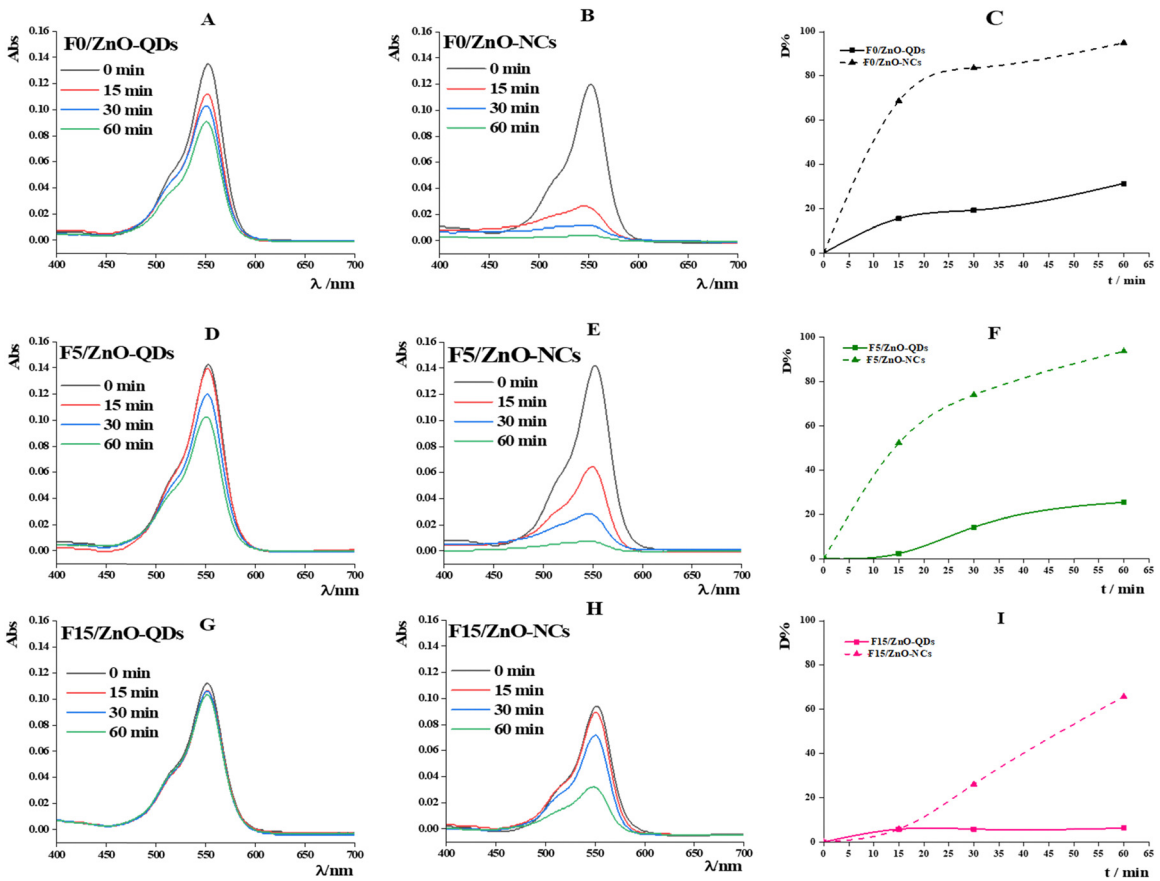

Fig. 6 Absorption spectra of the supernatants collected after the interaction of RhB solution with F0/ZnO-QDs (A), F0/ZnO-NCs (B), F5/ZnO-QDs (D), F5/ZnO-NCs (E), F15/ZnO-QDs (G), and F15/ZnO-NCs (H) at different times (black curve = time 0, red curve = 15 min, blue curve = 30 min, green curve = 60 min) under UV-vis irradiation. Degradation rate profiles over time for each couple of ZnO from different synthesis routes reported aside (C, F, and I).

Table 2 Summary of the estimated kinetic constants obtained by fitting the experimental trends

	0 order kinetics	1st order kinetics
Samples	k_0 (min^{-1})	k_1 ($\mu mol\ L^{-1}\ min^{-1}$)
F0/ZnO-NCs		0.097 ± 0.007
F0/ZnO-QDs	0.10 ± 0.01	
F5/ZnO-NCs		0.053 ± 0.001
F5/ZnO-QDs	0.082 ± 0.008	
F15/ZnO-NCs	0.17 ± 0.02	
F15/ZnO-QDs	0.028 ± 0.004	

then decreases by further increasing the fluorine content, with quantum yields of F15/ZnO-QDs and F20/ZnO-QDs lower than that of the undoped sample. So, for QDs with a size less than 4 nm, a minimum amount of dopant was sufficient and optimal to improve the optical properties of F/ZnO-QDs.

Photoactivity under UVA-light irradiation

The photoactivity of F/ZnO was evaluated by monitoring their ability to degrade Rhodamine B (RhB) selected as a model dye.[68] First, the pro-oxidant activity of nanocrystals was assessed in the dark and no RhB degradation was recorded. This result was in agreement with what was observed for preliminary pro-oxidative peroxidase (POD) and oxidase (OXD) mimicking assays, during which all the samples were inactive. This multiple evidence led to suppose that the production of free radicals had to be light-triggered.

Fig. 6 summarizes the results of photodegradation tests for undoped and F/ZnO at two significantly different fluorine contents (F5 and F15), as obtained from both synthetic routes, while Table 2 reports a summary of the estimated kinetic constants obtained by fitting the experimental trends.

By comparing the general trends, NCs produced by the solvothermal method were way more active than those produced through the wet-precipitation approach. In particular, the degradation of RhB was more intense for F/ZnO-NCs and this could be ascribable to a higher presence of defects in the crystalline structure. Indeed, as reported in the literature, the presence of intrinsic defects may intensify the photo(electro)chemical properties.[69,70] Specifically, oxygen vacancies V_O and zinc interstitials Zn_i could act as charge-carrier traps which delay the charge recombination. In addition, these defects may behave as surface sites facilitating the degradation of organic molecules through charge transfer interactions between the site and the analyte.[71] These results could be also explained by considering that the defects in the ZnO-NCs decreased the recombination of the excitons which turned into a lower emission intensity at higher F content, and also in agreement with luminescence results previously reported in literature.[24] It must be pointed out that the degradation efficiency of the nanocrystals with a higher content of fluoride decreased, this occurred because the fluoride had almost the same atomic radius as oxygen, so it could occupy the V_O decreasing the number of defects present in the structure. Finally, RhB concentration profiles over time were fitted to linear and exponential decay equations to identify the kinetic model suiting the most the photocatalytic behaviour of each nanosystem. In detail, F15/ZnO-NCs and all the photoactive nanosystems produced through wet-chemistry route exhibited 0-order kinetics, with the solvothermal one outperforming the others since exhibiting the highest k_0 (0.17 ± 0.02). Moreover, k_0 constant decreased with increasing nominal fluorine content. On the other hand, the best-performing F0/ZnO-NCs and F5/ZnO-NCs samples exhibited 1st order kinetics, with k_1 constant being again dependent on nominal fluorine content. Definitely, kinetic analysis was effective in further clarifying that the (i) solvothermal approach provided higher number of defects and active sites; (ii) wet-chemistry approach resulted in less photoactive nanomaterials, with saturated active sites even at such low RhB concentration (16.7 μM); and (iii) fluorine was particularly able in replacing oxygen in the lattices, reducing the number of defects and thus the charge transfer efficiency.

Conclusions

The study aimed to prepare colloidal fluorine-doped ZnO nanocrystals using two different synthesis strategies – wet-precipitation and solvothermal methods – with varying amounts of doping agent. The focus was to investigate how atomic doping, nanocrystal growth, and surface defects affect the optical behavior and photoactivity of F/ZnO. The research was conducted with a wide range of nominal atomic% of the doping agent (0–20) to understand how the properties of the nanocrystals could be simultaneously tuned as a function of the fluorine content and synthesis strategy employed. The wet-precipitation route led to the formation of very small quantum dots of about 3 nm in radius, showing good colloidal stability in suspension which was reduced by increasing the fluorine content as a consequence of the significant changes in the morphological and surface features induced by a greater amount of doping agent used during the synthesis. F/ZnO-QDs, obtained through the wet-precipitation method, exhibited scarce photoactivity and a significant fluorescence emission with the highest value of the relative quantum yield (Φ = 22%) for F/ZnO-QDs doped with a nominal concentration of fluorine of 5 at%. During solvothermal synthesis, nanocrystals are formed with varying shapes (from rod-like to spherical), sizes (ranging from 10 to 50 nm), and clustering tendencies that are strongly influenced by the presence of fluorine. These conditions result in low fluorescence emission, but high photoactivity is observed in F/ZnO with a low F content (5 at%), small size (approximately 10 nm in radius), and high surface defects. The photoactive efficiency of these nanocrystals can reach up to 95% after 60 minutes. This suggests a different growth of the crystalline structure and highlights the importance of controlling the fluorine content during the synthesis process. Definitely, this study allowed us to define the optimal conditions to alternatively design fluorescent F/ZnO-QDs for sensing and optoelectronic fields or photoactive F/ZnO-NCs for photocatalytic applications.

Data availability

Data for this article, including XRD and XPS data, are available at Zenodo repository at **https://doi.org/10.5281/zenodo.**

13144846. The data supporting this article have been also included as part of the ESI.†

Conflicts of interest

There are no conflicts to declare.

Acknowledgements

The work was supported by Programma per il Finanziamento della Ricerca di Ateneo (FRA) 2020, funded by the University of Naples Federico II, project title ''LPS-targeting nanostructured aptasensors for bacterial pathogens detection – LipAptaNanoSens'' (Cod. 000008 ALTRI_CdA_75_2021_FRA_LINEA_B-VITIELLO) and Fondo per il Programma Nazionale della Ricerca (PNR) e Progetti di Ricerca di Rilevante Interesse Nazionale (PRIN 2022), project title ''Glycolipids-coated colloidal quantum dots as optical biosensing platform for selective molecular recognition – GLYBIOSENS'', funded by the Italian Ministry of University and Research (MUR) and European Union – Next Generation EU, Mission 4, Component 2, Investment 1.1 – D.D. n. 104 del 02.02.2022, C.I. 2022PJP24F. This work has also received funding from the European Union's Horizon 2020 Research and Innovation Program under grant agreement No. 101007417, having benefitted from the access provided for experimental analyses by the CEA-LETI (Grenoble, France) within the framework of NFFA-Europe Pilot Transnational Access Activity (nffa.eu), proposal ID071.

References

1 S. Kargozar, S. J. Hoseini, P. B. Milan, S. Hooshmand, H.-W. Kim and M. Mozafari, *Biotechnol. J.*, 2020, **15**, 2000117.
2 H. Park, D. J. Shin and J. Yu, *J. Chem. Educ.*, 2021, **98**, 703–709.
3 N. X. Ca, N. T. Hien, X. Fan, P. V. Do, V. H. Yen, P. V. Hao, L. K. Quynh, T. T. T. Huong and V. X. Quang, *RSC Adv.*, 2023, **13**, 27292–27302.
4 H. Moon, C. Lee, W. Lee, J. Kim and H. Chae, *Adv. Mater.*, 2019, **31**, 1804294.
5 G. S. Selopal, H. Zhao, Z. M. Wang and F. Rosei, *Adv. Funct. Mater.*, 2020, **30**, 1908762.
6 W. Zhou, Y. Shang, F. P. García de Arquer, K. Xu, R. Wang, S. Luo, X. Xiao, X. Zhou, R. Huang, E. H. Sargent and Z. Ning, *Nat. Electron.*, 2020, **3**, 251–258.
7 P. Juzenas, W. Chen, Y.-P. Sun, M. A. N. Coelho, R. Generalov, N. Generalova and I. L. Christensen, *Adv. Drug Delivery Rev.*, 2008, **60**, 1600–1614.
8 A. C. S. Samia, X. Chen and C. Burda, *J. Am. Chem. Soc.*, 2003, **125**, 15736–15737.
9 P. Sun, Z. Xing, Z. Li and W. Zhou, *Chem. Eng. J.*, 2023, **458**, 141399.
10 A. Luchini, R. K. Heenan, L. Paduano and G. Vitiello, *Phys. Chem. Chem. Phys.*, 2016, **18**, 18441–18449.
11 A. Luchini, G. Vitiello, F. Rossi, O. R. D. Ballesteros, A. Radulescu, G. D'Errico, D. Montesarchio, C. de, J. Fernández and L. Paduano, *Phys. Chem. Chem. Phys.*, 2015, **17**, 6087–6097.
12 S. Brichkin and V. Razumov, *Russ. Chem. Rev.*, 2016, **85**(12), 1297–1312.
13 F. Chen, Q. Lin, H. Shen and A. Tang, *Mater. Chem. Front.*, 2020, **4**, 1340–1365.
14 A. Luchini, G. D'Errico, S. Leone, Z. Vaezi, A. Bortolotti, L. Stella, G. Vitiello and L. Paduano, *Colloids Surf., B*, 2018, **168**, 2–9.
15 A. Luchini, C. Irace, R. Santamaria, D. Montesarchio, R. K. Heenan, N. Szekely, A. Flori, L. Menichetti and L. Paduano, *Nanoscale*, 2016, **8**, 10078–10086.
16 R. Jiang, H. Wu, D. Manzani, W. Zhang and C. Liu, *Appl. Surf. Sci.*, 2023, **622**, 156931.
17 L. Zhang, L. Yin, C. Wang, N. Lun, Y. Qi and D. Xiang, *J. Phys. Chem. C*, 2010, **114**, 9651–9658.
18 J. Zhu, K. Lu, J. Li, Z. Liu and W. Ma, *Mater. Chem. Front.*, 2024, **8**, 1792–1807.
19 V. Kumar, J. Prakash, J. P. Singh, K. H. Chae, C. Swart, O. M. Ntwaeaborwa, H. C. Swart and V. Dutta, *Colloids Surf., B*, 2017, **159**, 191–199.
20 W. Li, G. Wang, C. Chen, J. Liao and Z. Li, *Nanomaterials*, 2017, **7**, 20.
21 K. Pradeev Raj, K. Sadaiyandi, A. Kennedy, S. Sagadevan, Z. Z. Chowdhury, M. R. B. Johan, F. A. Aziz, R. F. Rafique, R. Thamiz Selvi and R. Rathina Bala, *Nanoscale Res. Lett.*, 2018, **13**, 229.
22 J. Sowik, M. Miodyńska, B. Bajorowicz, A. Mikolajczyk, W. Lisowski, T. Klimczuk, D. Kaczor, A. Zaleska Medynska and A. Malankowska, *Appl. Surf. Sci.*, 2019, **464**, 651–663.
23 A. Arivarasan, S. Bharathi, S. Ezhil Arasi, S. Arunpandiyan, M. S. Revathy and R. Jayavel, *J. Lumin.*, 2020, **219**, 116881.
24 D. W. Bahnemann, Claudius Kormann and M. R. Hoffmann, *J. Phys. Chem.*, 1987, **91**, 3789–3798.
25 L. Spanhel, *J. Sol-Gel Sci. Technol.*, 2006, **39**, 7–24.
26 S. Das, P. Somu, A. K. Yadav, P. K. Hopke and S. Paul, *Environ. Sci.: Nano*, 2024, **11**, 739–765.
27 L. K. Jangir, Y. Kumari, A. Kumar, M. Kumar and K. Awasthi, *Mater. Chem. Front.*, 2017, **1**, 1413–1421.
28 X. Gong, H. Jiang, M. Cao, Z. Rao, X. Zhao and A. Vomiero, *Mater. Chem. Front.*, 2021, **5**, 4746–4755.
29 A. Agrawal, I. Kriegel and D. J. Milliron, *J. Phys. Chem. C*, 2015, **119**, 6227–6238.
30 M. Carofiglio, S. Barui, V. Cauda and M. Laurenti, *Appl. Sci.*, 2020, **10**(15), 5194.
31 A. Grala, M. Wolska-Pietkiewicz, Z. Wróbel, T. Ratajczyk, J. Kuncewicz and J. Lewiński, *Mater. Chem. Front.*, 2018, **2**, 1104–1111.
32 J. Huo, Y. Zhang, W. Kang, Y. Shen, X. Li, Z. Yan, Y. Pan and W. Sun, *Nanoscale Adv.*, 2023, **5**, 2846–2864.
33 G. P. Papari, B. Silvestri, G. Vitiello, L. De Stefano, I. Rea, G. Luciani, A. Aronne and A. Andreone, *J. Phys. Chem. C*, 2017, **121**, 16012–16020.
34 G. Vitiello, G. Iervolino, C. Imparato, I. Rea, F. Borbone, L. De Stefano, A. Aronne and V. Vaiano, *Sci. Total Environ.*, 2021, **762**, 143066.

35 Solution Methods for Metal Oxide Nanostructures – 1st Edition|Elsevier Shop, https://shop.elsevier.com/books/solution-methods-for-metal-oxide-nanostructures/mane/978-0-12-824353-4, (accessed 3 April 2024).
36 W. J. E. Beek, M. M. Wienk, M. Kemerink, X. Yang and R. A. J. Janssen, *J. Phys. Chem. B*, 2005, **109**, 9505–9516.
37 V. Venezia, M. Verrillo, N. Gallucci, R. Di Girolamo, G. Luciani, G. D'Errico, L. Paduano, A. Piccolo and G. Vitiello, *J. Environ. Chem. Eng.*, 2023, **11**(1), 108973.
38 N. Gallucci, M. Hmoudah, E. Martinez, A. El-Qanni, M. Di Serio, L. Paduano, G. Vitiello and V. Russo, *J. Environ. Chem. Eng.*, 2022, **10**, 107866.
39 N. Gallucci, G. Vitiello, R. Di Girolamo, P. Imbimbo, D. M. Monti, O. Tarallo, A. Vergara, I. Russo Krauss and L. Paduano, *Nanomaterials*, 2021, **11**, 542.
40 N. Gallucci, M.-S. Appavou, N. Cowieson, G. D'Errico, R. Di Girolamo, S. Lettieri, F. Sica, G. Vitiello and L. Paduano, *J. Colloid Interface Sci.*, 2024, **659**, 926–935.
41 G. Pota, N. Gallucci, D. Cavasso, I. Russo Krauss, G. Vitiello, F. Lopez-Gallego, A. Costantini and V. Califano, *Langmuir*, 2023, **39**(4), 1482–1494.
42 I. Romano, G. Vitiello, N. Gallucci, R. Di Girolamo, A. Cattaneo, A. Poli and P. Di Donato, *Microorganisms*, 2022, **10**, 1885.
43 S. Russo, M. Muscetta, P. Amato, V. Venezia, M. Verrillo, R. Rega, S. Lettieri, M. Cocca, R. Marotta and G. Vitiello, *Chemosphere*, 2024, **346**, 140605.
44 P. Amato, M. Muscetta, V. Venezia, M. Cocca, G. Gentile, R. Castaldo, R. Marotta and G. Vitiello, *J. Environ. Chem. Eng.*, 2023, **11**, 109003.
45 P. Wainer, O. Kendall, A. Lamb, S. J. Barrow, A. Tricoli, D. E. Gomez, J. van Embden and E. D. Gasparra, *Chem. Mater.*, 2019, **31**(23), 9604–9613.
46 A. Dakhlaoui, M. Jendoubi, L. S. Smiri, A. Kanaev and N. Jouini, *J. Cryst. Grow.*, 2009, **311**, 3989–3996.
47 Y. Yang, Y. Jin, H. He, A. Wang, Y. Tu, H. Lu and Z. Ye, *J. Am. Chem. Soc.*, 2010, **132**(38), 13381–13394.
48 R. Buonsanti and D. J. Milliron, *Chem. Mater.*, 2013, **25**(8), 1305–1317.
49 Y. Guo, S. Wuttke, A. Vimont, M. Daturi, J.-C. Lavalley, K. Teinz and E. Kemnitz, *J. Mater. Chem.*, 2012, **22**, 14587–14593.
50 A. Zuber, M. Purdey, E. Schartner, C. Forbes, B. van der Hoek, D. Giles, A. Abell, T. Monro and H. Ebendorff-Heidepriem, *Sens. Actuators, B*, 2016, **227**, 117–127.
51 N. Ahmed, J. Singh, H. Chauhan, P. Gupta, A. Anjum and H. Kour, *Int. J. Food Nutr. Saf.*, 2013, **4**, 34–42.
52 E. G. Goh, X. Xu and P. G. McCormick, *Scr. Mater.*, 2014, **78–79**, 49–52.
53 J. Singh, A. Rathi, M. Rawat, V. Kumar and K.-H. Kim, *Composites, Part B*, 2019, **166**, 361–370.
54 T. M. Hammad, J. K. Salem and R. G. Harrison, *Appl. Nanosci.*, 2013, **3**, 133–139.
55 H. Saadi, F. I. H. Rhouma, Z. Benzarti, Z. Bougrioua, S. Guermazi and K. Khirouni, *Mater. Res. Bull.*, 2020, **129**, 110884.
56 E. Y. Shaba, J. O. Jacob, J. O. Tijani and M. A. T. Suleiman, *Appl. Water Sci.*, 2021, **11**, 48.
57 I. H. Ifijen, M. Maliki and B. Anegbe, *OpenNano*, 2022, **8**, 100082.
58 M. Samadi, M. Zirak, A. Naseri, E. Khorashadizade and A. Z. Moshfegh, *Thin Solid Films*, 2016, **605**, 2–19.
59 P. K. Samanta, *Optik*, 2020, **221**, 165337.
60 J. Oliva, L. Diaz-Torres, A. Torres-Castro, P. Salas, L. Perez-Mayen and E. D. la Rosa, *Opt. Mater. Express*, 2015, **5**, 1109–1121.
61 A. Sahai and N. Goswami, *Ceram. Int.*, 2014, **40**, 14569–14578.
62 G. Sico, M. Montanino, M. Ventre, V. Mollo, C. T. Prontera, C. Minarini and G. Magnani, *Scr. Mater.*, 2019, **164**, 48–51.
63 O. W. Kennedy, E. R. White, A. Howkins, C. K. Williams, I. W. Boyd, P. A. Warburton and M. S. P. Shaffer, *J. Phys. Chem. Lett.*, 2019, **10**, 386–392.
64 H. Parangusan, D. Ponnamma and M. A. A. Al-Maadeed, *Bull. Mater. Sci.*, 2019, **42**, 179.
65 W. Yang, H. Yang, W. Ding, B. Zhang, L. Zhang, L. Wang, M. Yu and Q. Zhang, *Ultrason. Sonochem.*, 2016, **33**, 106–117.
66 R. Raji and K. G. Gopchandran, *J. Sci.: Adv. Mater. Devices*, 2017, **2**, 51–58.
67 A. B. Djurišić, Y. H. Leung, K. H. Tam, L. Ding, W. K. Ge, H. Y. Chen and S. Gwo, *Appl. Phys. Lett.*, 2006, **88**, 103107.
68 V. Venezia, M. Verrillo, N. Gallucci, R. Di Girolamo, G. Luciani, G. D'Errico, L. Paduano, A. Piccolo and G. Vitiello, *J. Environ. Chem. Eng.*, 2023, **11**, 108973.
69 F. Liu, Y. H. Leung, A. B. Djurisic, A. M. C. Ng and W. K. Chan, *J. Phys. Chem. C*, 2013, **117**(23), 12218–12228.
70 F. Kayaci, S. Vempati, I. Donmez, N. Biyikli and T. Uyar, *Nanoscale*, 2014, **6**, 10224–10234.
71 J. Kegel, V. Z. Zubialevich, M. Schmidt, I. A. Povey and M. E. Pemble, *ACS Appl. Mater. Interfaces*, 2018, **10**(21), 17994–18004.